CrossMark

Fabrication and Characterization of Nanoporous Silicon Relative Humidity Sensors

S. Oguz Aytekin[1] · R. Ince[2]

Abstract This work describes a porous, silicon-based humidity sensor operating under the capacitive transduction principle. One of the aims of this work is to determine the main parameters such as sensitivity, linearity, hysteresis, and time response to step humidity changes of four samples via measurements of their capacitance. The parameters gauged by capacitance measurements were used to explain the dynamics of its operation. The most sensitive sample caused changes in relative humidity of 74 nF·%rh^{-1}. Hysteresis of at least 3.6 % to 4.6 % was found to occur. Humidity sensor samples synthesized from nanoporous silicon were also analyzed by scanning electron microscopy, image processing, and Raman spectra red shifts. As a result of these measurement and analysis of this work, the best synthesis conditions and nanopore surface and sub-surface diameters for producing high performing humidity sensors were identified. Another aim of this work is to find the optimal pore size from the analysis of image processing and Raman spectra. The optimal porous sizes in relation to the analyzed sensor's characteristics were found to be between 4 nm and 26 nm. The novelty of this work is to establish the relationship between the capacitance measurements with image processing of SEM images and Raman spectral measurements. The mechanical stability of the samples was also gauged over 3 months utilizing both capacitance and Raman spectral measurements.

✉ S. Oguz Aytekin
seda.aytekin@tubitak.gov.tr

R. Ince
rince@yeditepe.edu.tr

[1] TUBITAK UME, TUBITAK Gebze Yerleskesi, Dr. Zeki Acar Cad, No.1, 41470 Gebze, Kocaeli, Turkey

[2] Department of Physics, Yeditepe University, Kayışdağı Cad., Kayışdağı/Erenköy, 34755 Istanbul, Turkey

1 Introduction

Humidity metrology is a critical requirement in science: hydrology, environmental
studies, meteorology, and forecasting for climate studies. In addition, it has a wide
range of applications in society: the food processing industry, air-conditioning, and
horticulture to name a few. Primary humidity metrology service requires mainte-
nance, realization, and dissemination of humidity parameters which must be closely
monitored along with temperature [1–4]. For industrial applications, humidity mea-
surements are made mostly with sensors made from porous ceramic and polymer
materials. Porous silicon is a good alternative to these materials since the sensor ele-
ment and electronics can easily be integrated on the same chip.

The porous silicon structure was first discovered at Bell Laboratory by Uhlirs in
the mid-1950s [5]. It was not studied in detail until the discovery of room-temperature
photoluminescence by Canham [6,7] in 1990. Porous silicon (PSi) structures have
been extensively studied since then. Although, as a result of room-temperature pho-
toluminescence, silicon was thought to be mainly useful for optoelectronic processes,
it found application areas including biotechnology, energy storage, solar technology,
optics, sensing of humidity, methanol, and other gases. Porous silicon is utilized as a
sensor material due to its immense surface-to-volume ratio for gas or humidity sensing
[8–13].

Nanoporous silicon (NPS) can be formed from a silicon wafer substrate by anodiza-
tion with hydrofluoric acid (HF) in an anodization cell for up to a few hours. Variations
in the substrate parameters and variations in the forming parameters of the anodization
process provide an opportunity to obtain a variety of internal nanostructures in a myriad
of shapes, spherical, column, fractal, or sponge-like within a silicon substrate. Silicon
wafer substrate parameters include doping concentration, resistivity, and orientation.
Formation parameters of NPS include anodization current density, anodization time,
concentration of HF, and temperature [14–19].

The current state of the art of humidity sensors based on sensing materials includes
electrolytes, polymers, and ceramics. These types of humidity sensors are character-
ized in terms of their resistive (impedance) or capacitance responses. Most humidity
or relative humidity (RH) sensors rely on capacitance sensing, since humidity changes
the permittivity of the sensing dielectric across electrodes deposited at opposite faces
of the sensor.

Nanoporous sensors based on silicon can be a good candidate for a humidity sensing
material due to their tunability during fabrication. The samples possessed various pore
diameters, with longer anodization times during sample preparation giving rise to
larger diameter nanocrystals. On the other hand, the main feature that must be resolved
is structural degradation. Structural degradation was improved by implementing a new
drying procedure to the NPS samples. Otherwise, the whole structure was collapsed
just after the anodization process.

Capacitance measurements are the main characterization technique to be conducted to determine the main characteristics of humidity sensors, which requires a rather complicated measurement setup compared with spectroscopic measurements. In this work, capacitance measurements were performed in order to determine the sensitivity, linearity, hysteresis, and time response to step humidity changes of porous silicon samples. The novelty of this work is to establish the relationship between the capacitance measurements with image processing of SEM images and Raman spectral measurements, and to find the optimal pore size from the analysis of image processing and Raman spectra.

Characterization of porous silicon using Raman spectroscopy has been studied extensively dating back to 1979 [20–24]. More recently, Raman analysis has been employed to determine the dimensions of silicon nanocrystals (SNC) in NPS [25–35]. In this work, structural characterization of NPS samples was conducted using both, Raman spectroscopy, and scanning electron microscopy (SEM) techniques. SEM images provide information about the nanopore pattern features; dendrite type, channel formations, and side branches [14,15,36,37]. The purpose of this work is to determine the optimal pore size and the size distribution of the nanopore diameters in each sample using both Raman spectra and SEM processed images of the samples. This information will then be compared with the characteristics of each sample (linearity, sensitivity, response time, and hysteresis) determined from capacitance measurements over the relative humidity range from 20 %rh to 95 %rh.

Raman spectroscopy and SEM analysis in terms of structural parameters such as diameters of granular silicon islands and holes which are in the nanometer range were performed. Comparison of spectroscopic parameter analysis with capacitance measurements was also conducted and found to be in good correlation. Therefore, it can be stated that Raman spectroscopy together with SEM techniques is an alternative to the capacitance characterization technique. The main aim of this paper is to present that the spectroscopic characterization techniques implemented to NPS samples were found to be less expensive and uncomplicated than the capacitance characterization technique.

Derived from Knudson diffusion, the Kelvin equation gives the basis for calculation of optimum pore size as a function of relative humidity. According to the Kelvin equation, the ideal pore sizes required for sensing of relative humidity values from 20 %rh to 95 %rh range from 0.8 nm to 40 nm, respectively. Utilizing SEM and Raman analyses, it was determined that the pore dimensions produced in the anodization of the silicon wafer were within this range.

2 Theory

2.1 Capacitance

Porous silicon humidity sensor was designed as a capacitive sensor; thus, a humidity sensitive porous silicon material is placed between two metallic plates which are vacuum-coated with aluminum. The top structure is designed as an interdigitated electrode; the bottom surface is fully covered by aluminum. This structure resembles

the typical capacitor device which consists of two conducting plates separated by a dielectric medium.

The top electrode must have an interdigitated structure (constructed of separate metal lines of gap ≈0.25 mm) to allow water through the empty spaces between. Since the composition of the NPS dielectric depends on water concentration, the electrical permittivity varies, causing the sensed capacitance to change with percent relative humidity. In essence, the sensor with deposited electrodes acts as a parallel-plate capacitor with a variable dielectric constant, ε, due to water molecules adsorbing onto the NPS surface from the ambient air.

The parallel-plate capacitance of a material is

$$C = \varepsilon A / d \tag{1}$$

A series combination of capacitors C_i which causes an equivalent capacitance is

$$C_{\text{Series}} = 1 / \sum\nolimits_i (1/C_i.) \tag{2}$$

A parallel combination of capacitors which causes an equivalent capacitance is

$$C_{\text{Parallel}} = \sum\nolimits_i C_i. \tag{3}$$

The equivalent capacitance of the sensors is considered to be a combination of these networks since the porous silicon layer can be regarded as a complicated dielectric material generally [38].

Three layers are present in the NPS samples: a very thin surface NPS layer into which water diffuses, a thin sub-surface NPS layer free of water, and a much thicker bottom crystalline silicon wafer layer. The latter has no observable NPS in Fig. 1a, so it is assumed that the etching solution did not penetrate the bottom of the wafer. Images from Fig. 1a reveal the depth of NPS to range from $d_{\text{NPS}} = 2.7\,\mu\text{m}$ to $13.9\,\mu\text{m}$, increasing with anodization time.

2.2 Raman Spectra of Nanocrystals

In crystalline solids, the Raman effect is caused by phonons. There is an incident photon–electron interaction followed by an electron–lattice interaction. An incoming photon excites an electron, causing an excited electron–hole pair. The latter is scattered at the lattice, inducing a phonon in the solid and causing the electron–hole pair to return to the original state by emitting a photon. The latter is reduced in energy compared to the incident photon by the amount lost in the scattering event.

For every crystal symmetry class, it is possible to calculate which phonons are Raman active, and in which measurement geometry, i.e., for which direction of polarization of the incident and scattered light, relative to the crystallographic axis. In nanocrystalline materials, the phonons are of similar dimensions to the nanostructures, and so are confined. As a result, Raman spectra display the macro-size crystalline Raman features broadened and shifted by phonon confinement.
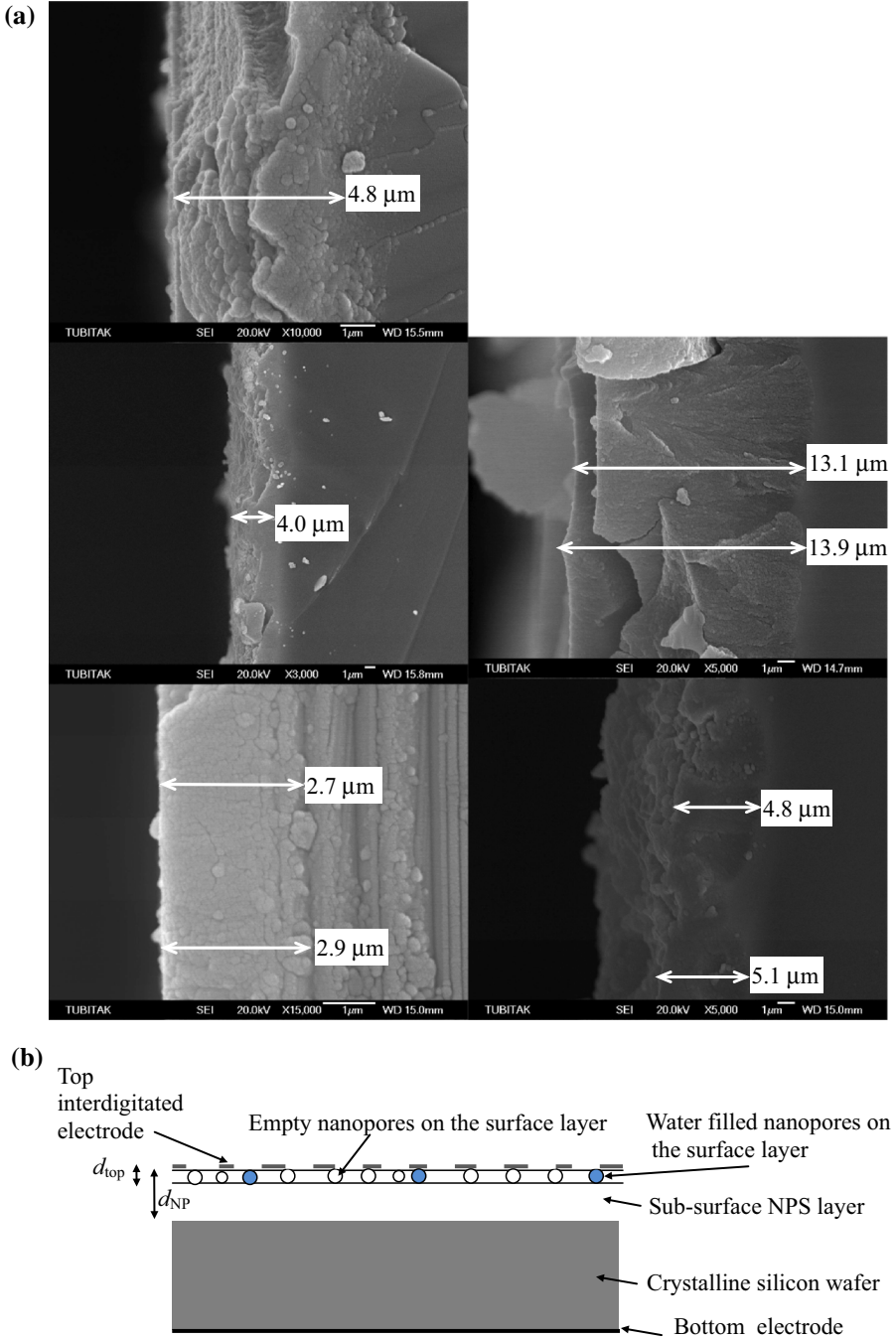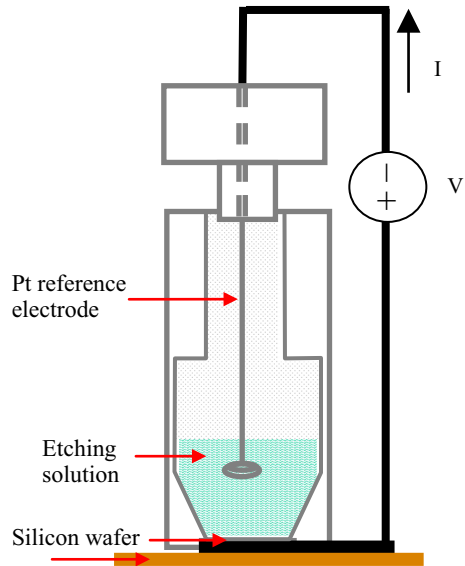
Fig. 1 (a) Cross-section SEM images obtained from samples A1, A2, A3, A4, and A5 and (b) a typical humidity NPS sensing sample structure modeled on Fig. 2a

Fig. 2 Drawing of Teflon cell
used for anodization of samples

Nanometer-sized silicon structures are known to exhibit red-shifted Raman spectra
[23,24,28,29,35,39,40]. By using an adequate model, it is possible to estimate the
size of the nanocrystals [23,28,29,41,42].

3 Experimental Apparatus and Procedures

3.1 Specimens and Formation Parameters

A drawing of the electrochemical anodization setup used to produce porous silicon
structures on p-type silicon wafers having a resistivity of 1 Ω·cm to 20 Ω·cm and (1
0 0) orientation is shown in Fig. 2. The anodization setup was composed of a Teflon
anodization cell, a platinum electrode, an anodization solution having hydrofluoric acid
and ethanol, and a current source meter. The wafer was cleaned with a standard wafer
cleaning method (RCA method) which was discovered by Kern while working for
RCA, the Radio Corporation of America. The unpolished side of the wafer was coated
with aluminum by the vacuum evaporation technique. The samples were then annealed
in an oven at 400 °C for 30 min to make ohmic contacts. The silicon substrate was
then diced into equal pieces and placed in the homemade Teflon anodization cell. The
silicon was mounted as an anode on the bottom of the anodization cell and completes
the electrical circuit by putting a spiral-shaped platinum wire as a cathode in a parallel
way to achieve a homogeneous structure throughout the porous silicon.

The porosity, i.e., the void fraction in the porous layer, is determined by the current
density (about 10 mA·cm^{-2} to 100 mA·cm^{-2}), composition of electrolyte, resistance,
and the doping density of the silicon substrate.

10 ml hydrofluoric (HF) acid of 48 % in concentration and 10 ml ethanol were mixed and poured into the homemade anodization cell. A current density of 5 mA·cm^{-2} was passed through the wafer for time durations of 15 min, 30 min, 45 min, 60 min, and 75 min. The samples were labeled A1, A2, A3, A4, and A5, respectively. Pentane drying was applied to all of the samples to prevent cracking of the porous structure due to evaporation of water from nanopores. A detailed description of the experimental procedure for the formation of porous silicon samples using a homemade anodization system is presented elsewhere [43].

3.2 Characterization Techniques

3.2.1 Scanning Electron Microscopy (SEM) and Processing of SEM Images

SEM is a non-destructive method, which probes the surface area of the material; it has a 10 nm resolution for porous silicon samples.

A JEOL 6335F scanning electron microscope (SEM) was used to obtain the surface and cross-sectional images of the porous silicon samples. The SEM images of the porous samples were obtained with a magnification of 75 000 throughout this work.

Cross-sectional SEM images of the five sample wafers (presented in Fig. 2a) reveal the structure shown in Fig. 2b. The porous silicon structure depths within the samples range from 2.7 μm to 13.9 μm out of the total wafer thickness of 500 μm.

Size distributions, including the diameter of nanometer-sized silicon crystalline islands or granules, were determined from an algorithm developed in the MATLAB Image Processing Toolbox. The algorithm was based on the use of the 'Granulometry' function, which determines the size distribution of objects in an image. Dimensions of image details were determined by sifting them through a circular structuring element of increasing size [44]. Images of the SNC obtained are presented in Fig. 3a. In all SEM images, it was observed that the SNC dimensions were similar to the SNP dimensions. This assumption was used throughout this work, and is also evident from the images of Figs. 2a and 3a. The size distributions of each image from Fig. 3a were determined from the algorithm described; they are presented in Fig. 3b.

3.2.2 Raman Spectroscopy

Raman spectroscopy is a non-destructive method that has a probing volume which depends on the laser wavelength, laser spot size, and the beam penetration depth. It probes a volume of the material with a resolution of 1 nm [25–35]. A Raman microscope (Renishaw inVia) was used to obtain Raman spectra of all the samples. The laser power was set to 5 mW during Raman spectra measurements in order to avoid heating the samples. Raman spectroscopy measurements were carried out with a laser having an excitation wavelength of 514 nm which has a penetration depth of approximately 500 nm in silicon, together with a 2 μm laser spot diameter resulted in a probing volume of approximately 1 μm^3.

Dimensions for silicon spheres, calculated by Lu et al. [35], range from 1.4 nm to 4.9 nm. It is assumed that the calculation of the size of the spheres can be extended up
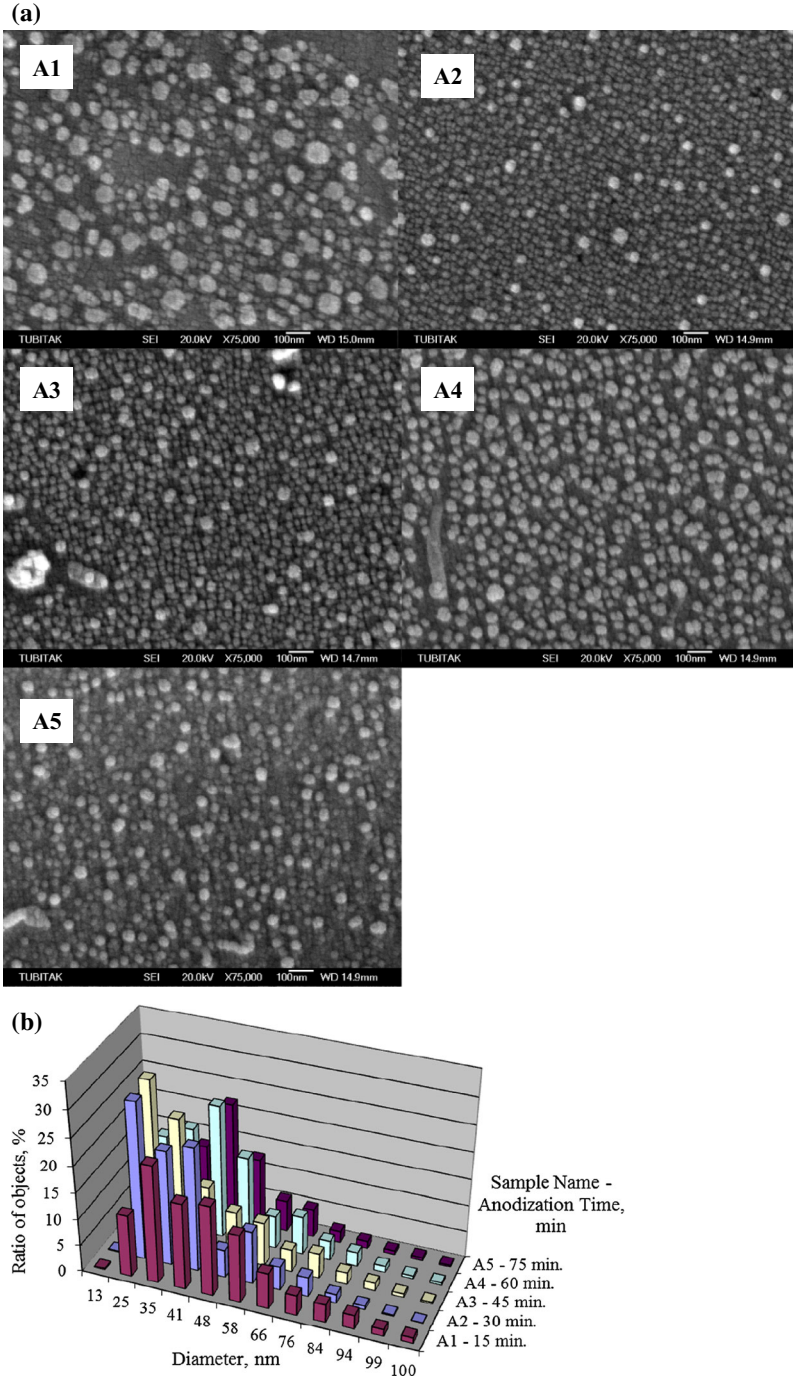
(a)

(b)

Fig. 3 (a) SEM surface images at magnifications of 75 000 and (b) size distribution of SNC diameters obtained from Fig. 3a images using MATLAB. Diameter versus ratio of objects in image

to 16 nm according to the results obtained from Faraci et al. [23]. The Richter equation was also used to show an asymmetric Raman spectrum line shape and wavenumber downshifts with decreasing nanowire diameter from 20 nm to 3 nm [42]. The Richter equation, which is assumed to approximate well up to 20 nm, is used throughout this paper.

$$\Delta\omega = \omega_{\mathrm{PSi}} - \omega_{\mathrm{cSi}} = -A \cdot (a/L)^{\gamma} \qquad (4)$$

ω_{PSi} (cm^{-1}) and ω_{cSi} (521 cm^{-1}) are the characteristic Raman band positions of porous silicon nanocrystallites and c-Si, respectively. For spherical Si nanocrystallite, $A = 47.41$ cm^{-1}, $\gamma = 1.44$ [24]. "a" is the lattice constant of silicon and is equal to 0.543 nm, and L is the trap dimension, i.e., the diameter of the SNC.

3.2.3 Capacitance Measurements

Capacitance measurements were carried out with an LCR meter (7600 from QuadTech) at a frequency of 1 kHz in a thermally isolated chamber of a humidity generator from Thunder Scientific. The humidity generator is a primary standard which possesses an annual drift of 0.3 %rh.

Relative humidity sensors are characterized mostly in terms of their sensitivity, linearity, and capacitance change [45,46]. NPS relative humidity sensors are characterized in terms of the normalized percentage capacitance change (*NPCC*) in the range from 20 %rh to 95 %rh [45]. The normalized percentage capacitance change was calculated using Eq. 5 below, and listed in Table 1. Two of the sensor samples, A2 and A4, were broken during measurements, so only the three remaining samples (A1, A3, and A5) were used for final measurements at a temperature of 23 °C.

$$NPCC_{\%\mathrm{RH}} = \left((C_{\mathrm{RHhigh}} - C_{\mathrm{RHlow}})\big/C_{\mathrm{RHlow}}\right) \cdot \left(1\big/\Delta RH\right) \cdot 100, \qquad (5)$$

where *NPCC* is the normalized percentage capacitance change, ΔRH is the relative humidity change, $\Delta RH = RH_{\mathrm{high}} - RH_{\mathrm{low}}$, RH_{high} is the highest relative humidity value, RH_{low} is the lowest relative humidity value, C_{RHhigh} is the capacitance at the highest relative humidity value, and C_{RHlow} is the capacitance at the lowest relative humidity value.

Sensitivity values of sensors were calculated using Eq. 6 as given below and from the measured capacitance values in the above specified relative humidity range. The calculated sensitivity values are listed in Table 1.

$$S = \left(C_{\mathrm{RHhigh}} - C_{\mathrm{RHhigh}}\right) \cdot (1/\Delta RH) \cdot 100, \qquad (6)$$

where S is the sensitivity.

Capacitance measurements also gauge the quality of the mechanical structure of the NPS layers. This is critically important, since it determines the time period over which the sensor can be reliably utilized. Thus, after the measurements were completed on each sample, they were kept at ambient conditions for 3 months and their performance over the humidity range was again determined to gauge their mechanical stability over time as depicted in Fig. 4.

Table 1 Capacitance values of porous silicon relative humidity sensors at different anodization times

Sample number	Anodization time (min)	Capacitance values of NPS samples at 23 °C			$NPCC^a$ ($\%rh^{-1}$)	Sensitivity (nF·$\%rh^{-1}$)
		At 20 %rh (nF)	At 50 %rh (nF)	At 95 %rh (nF)		
A1	15	13.45	37.50	63.18	4.93	66.3
A3	45	10.49	24.02	66.30	7.09	74.4
A5	75	0.49	5.43	34.22	91.78	44.9

[a] Normalized percentage capacitance change
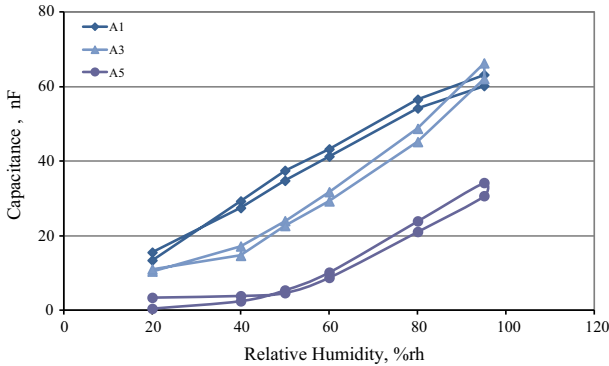
Fig. 4 Hysteresis measurements of nanoporous relative humidity sensors
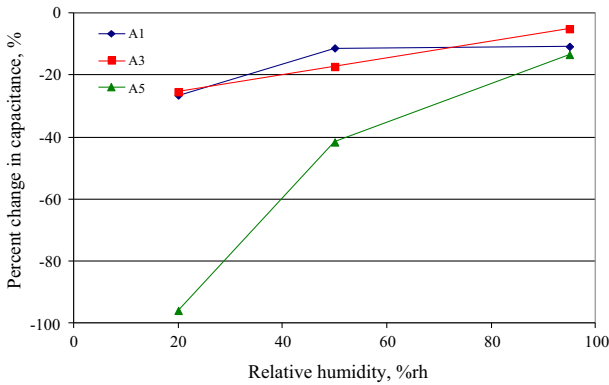

Fig. 5 Mechanical degradation gauged via percentage change in capacitance over 3 months

Hystereses of the samples were calculated using the experimental results which include two consecutive measurements starting from 20 %rh to 95 %rh as depicted in Fig. 5. The maximum value of the differences calculated at each relative humidity value was considered as hysteresis of the sample.

4 Results

4.1 SEM Images

The average SNC diameters of each sample in Fig. 3b were plotted on the left-hand axis against anodization time in Fig. 6; these also indirectly describe the average nanopore diameters.

Using the Raman spectral shifts, the diameters of SNC were calculated from Eq. 4 and are displayed on the right-hand axis of Fig. 6. Although the determined values were almost fivefold disparate in comparison with the left-hand axis results of SEM, the trend in the diameters was well correlated, as evident in Fig. 6. This dimensional disparity is caused by the different resolutions of the two methods: 10 nm for SEM and
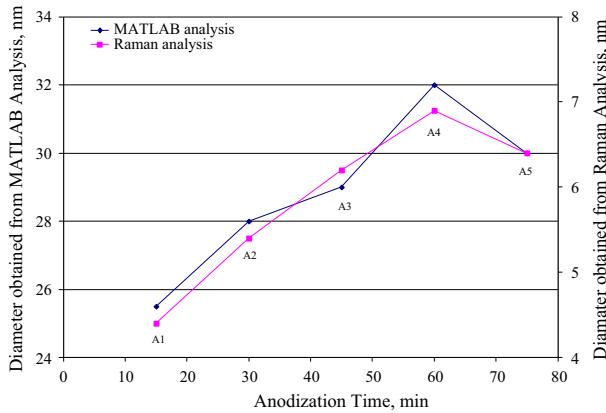
Fig. 6 Diameter values of samples produced at different anodization times obtained from MATLAB image processing and Raman spectrometry

1 nm for Raman spectroscopy. In addition, the image processing can only determine spherical shapes with well-defined edges on the sample surface. Raman spectroscopy can probe much deeper below the surface. In the SEM images of Fig. 7, 25 nm to 40 nm diameter granular islands are composed of tiny islands having much smaller diameters. Except for A1, they show that the SNC diameters are smaller at the bottom, but larger at the top of the samples; this is likely to also be the case for the nanopores. This is usual in NPS structures, since there are basically two independent formation mechanisms which may coexist simultaneously. This results in a superposition of structures of nanometer-to-micrometer-sized pores [42,47]. This explains why Raman spectroscopy, a sub-surface technique, determined smaller average SNC diameters, implying smaller nanopores.

Figure 6 shows that SNC diameters increase linearly with anodization time, since the other parameters were kept constant: anodization current density (5 mA·cm^{-2}) and concentration of anodization solution) (1:1 volume per volume (v/v) mixture of hydrofluoric acid 48 mass% in water and ethanol).

In Fig. 6, although SNC diameters are observed to increase with time, for both SEM and Raman determinations, they suddenly decrease on samples treated for more than 60 min. This can be explained by the characteristics of electrochemical anodization, where a longer permeance time of silicon in HF solution results in a higher mass of chemically dissolved silicon. Thus, as d_{NPS} increases, diffusion of HF acid may start to limit the growth rate as it carries the dissolved silicon away from the surface layer.

Anodization times for each sample and their corresponding NPS layer thicknesses are shown in Fig. 8. Here sample A5 has a structure in which d_{top} penetrates all the way into the sub-surface region, completely occupying d_{NPS}. This is related to a more open structure, where more of the silicon has been dissolved and removed, perhaps by diffusion with HF away from the sensing layer, leaving a percolation region with a smaller SNC and a larger average nanopores [48]. Evidently as the anodization time increases, so does the thickness of the NPS; this is also the case in the literature.
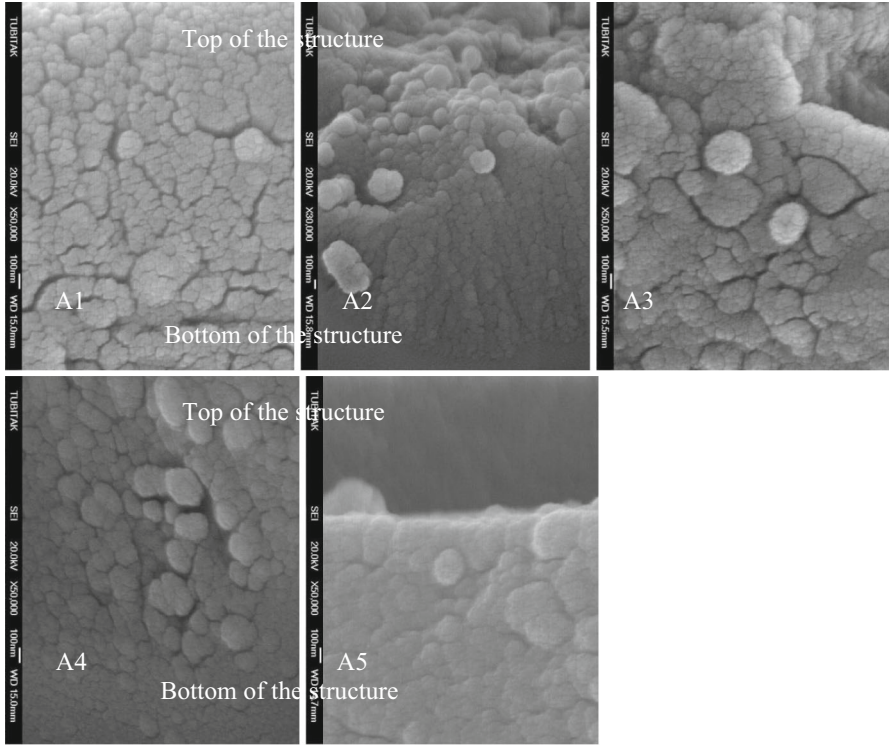
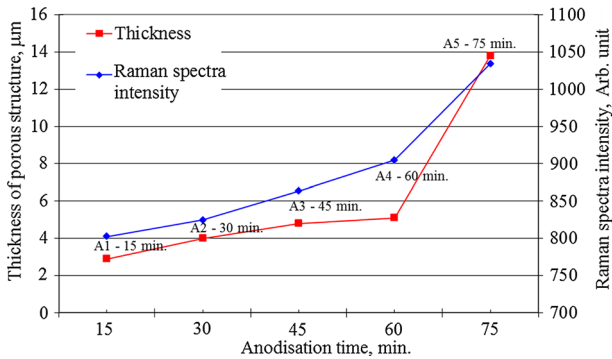**Fig. 7** Cross-sectional images of porous silicon samples

Fig. 8 Thickness of porous silicon structures at varying anodization times

4.2 Raman Spectra

Raman spectra of each sample A1–A5, at the same current density (5 mA·cm^{-2}), but at varying anodization times (from 15 min to 75 min) are given in Fig. 9 for all five samples. Raman spectra are given with respect to the spectrum of crystalline silicon (c-Si) 521 cm^{-1} [23], shown as a green curve in the graphs. Here red (down) shifts in
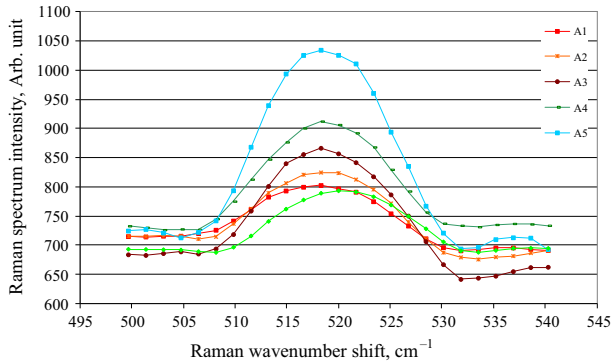
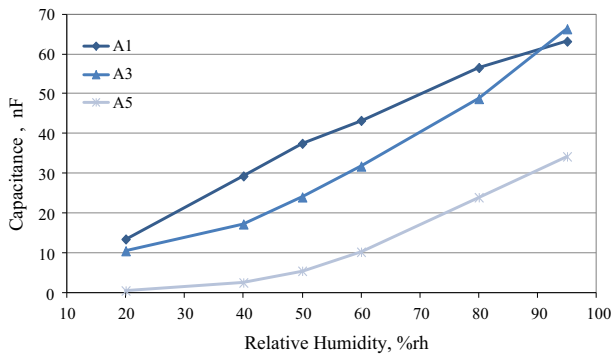**Fig. 9** Raman spectra from samples of set1 and the crystalline silicon

Fig. 10 Capacitance versus relative humidity values of nanoporous relative humidity sensors

the optical phonon mode occur after porous silicon formation due to phonon confinement; this was used to calculate the SNC diameters. Figure 9 also shows enhancement of the Raman peak intensity, further evidence of nanocrystal formation [49–51].

4.3 Capacitance Measurements

Capacitance versus relative humidity measurements from 20 %rh to 95 %rh were performed in the chamber of a humidity generator from Thunder Scientific. A dry condition was accomplished in a desiccator fed by laboratory-grade nitrogen gas stream with relative humidity ranges from 3 %rh to 5 %rh.

The measured capacitances of the five samples versus humidity in the range from 20 %rh to 95 %rh are presented in Fig. 10.

Clearly, sample A1 has a sensor structure and pore dimension which allows d_{top} to decrease gradually enough to produce a linear capacitance response to relative humidity change; this is expected from a structure with smaller pore dimensions, since it would be harder for the water droplets to move during diffusion.
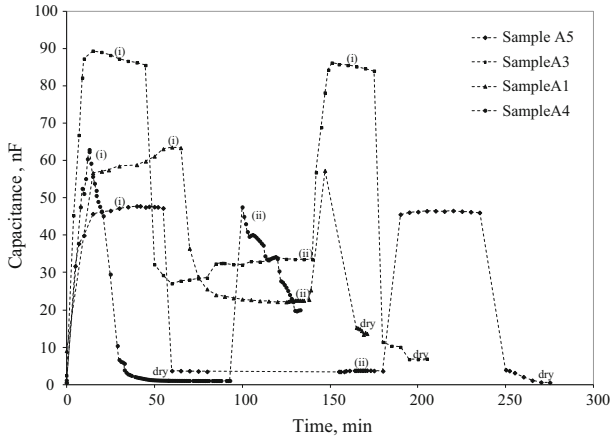
Fig. 11 Response time of the NPS sensors: dry = nitrogen gas has dried the sample; (i) 95 %rh and (ii) 50 %rh.

Table 2 Sensor time responses to 63 % increase and decrease in step relative humidity changes

Sample number	Step increase (%rh)	Response ($s \cdot \%rh^{-1}$)	Step decrease (%rh)	Response ($s \cdot \%rh^{-1}$)
A1	5–95	5.9	95–50	33.3
A3	5–95	3.6	95–50	6.7
A4	5–95	4.4	95–50	8.9
A5	5–95	3.1	95–50	4.5

Table 1 shows sample A3 to be the most sensitive to changes in relative humidity ($74 \ nF \cdot \%rh^{-1}$), followed closely by sample A1. Figure 10 shows sample A1 to display the most linear capacitance response over the relative humidity range; the other sensor characteristics were then investigated.

The response time of sensor samples (A1, A3, A4, and A5) to humidity changes from dry conditions within a sealed desiccator to 95 %rh and then 50 %rh is shown in Fig. 11. The response times for reaching 63 % of the step humidity function are shown in Table 2. The fastest response is displayed by sample A5 at $3.1 \ s \cdot \%rh^{-1}$, the slowest response is displayed by sample A1; degrading sixfold for step decreases. Degradation in response time of the other samples to a step decrease in humidity was between one- and twofold. This occurs because nitrogen gas must reach the inner smaller dimension nanopores (4.5 nm on average) to desorb the water droplets [48]. Since sample A1 has the smallest pore diameters, this process will be more difficult to achieve. The diameter of SNP of Sample A5 suddenly decreases, with anodization time as shown in Fig. 6. This corresponds with an increase in the nanopore diameter, as the material is dissolved in HF acid. Thus, larger pores would allow nitrogen gas to enter more easily for drying purposes and give rise to the greater response time observed for both step increase and decrease in relative humidity.

Table 3 Mechanical degradation gauged via decrease in capacitance of samples

Sample number	Anodization time (min)	Capacitance values of samples after 3 months at 23 °C[a]		
		At 20 %rh (nF)	At 50 %rh (nF)	At 95 %rh (nF)
A1	15	9.89 (−26.5)	33.26 (−11.3)	56.36 (−10.8)
A3	45	7.83 (−25.4)	19.86 (−17.3)	62.92 (−5.1)
A5	75	0.02 (−95.9)	3.17 (−41.6)	29.63 (−13.4)

[a] % decrease in capacitance is in parentheses

Since relative humidity calibration starts from the lowest relative humidity to the highest relative humidity value, hysteresis was also determined from the consecutive measurements of relative humidity values as given (20-40-50-60-80-95-95-80-60-50-40-20) %rh. Hystereses of all three samples were investigated, and the results are shown in Fig. 4. Sample A1 had the lowest hysteresis of ~3.3 % compared to samples A3 and A5 with hysteresis of about 4.6 %; all of these were worst cases occurring at 95 %rh.

In order to gauge the mechanical stability over time, each sensor was carefully stored at room temperature around 23 °C and room relative humidity around 45 %rh for 3 months, and they then had their capacitance determined once again. The results are presented in Table 3. Mechanical degradation of porous silicon relative humidity sensors in percentage was calculated from this capacitance change over 3 months, as shown in Fig. 5.

Considering all the factors, A1 performed the best for linearity and also had the least hysteresis. Both A1 and A3 had the best mechanical stability, although A3 was about 11 % more sensitive.

5 Conclusion

It was shown that the image processing of SEM images developed in this work was successful at determining and sizing surface features. An increase in Raman spectral intensity was reliable evidence for the development of silicon nanocrystals during anodization. Raman spectral red shifts were found to provide data which were reliable enough to compute sub-surface SNC dimensions. The SNC diameter within the NPS sensor region increases with anodization time up until 60 min; at longer anodization times, the diameter suddenly decreases. Both SEM image processing and Raman spectral determinations exhibit the same trend with a high degree of correlation, demonstrating that both surface and sub-surface SNC exhibit the same behavior.

The SEM images show that the SNC form as uniform spheres of similar dimensions to the nanopores between them. This can only occur when the silicon crystal is dissolved by HF and allowed to re-crystallize as nanocrystals; the permeance time of anodization allows the nanocrystals time to grow. Thus, longer anodization times are associated with larger diameter SNC. However, after 60 min, the SNC diameter decrease of sample A5 corresponds to a limiting mechanism for the nanocrystal growth

rate. This may be caused when a higher mass of chemically dissolved silicon is carried away by diffusion of HF acid, since the sub-surface NPS layer also deepens with the anodization time. This may start to limit the nanocrystal growth rate, but causing much larger pores, resulting in a highly percolated structure. This seems to be borne out by the capacitance measurements also.

Sample A3 was the most sensitive to changes in relative humidity (74 nF·%rh^{-1}), followed closely by sample A1. However, sample A1 displayed the most linear capacitance response.

It was found that a lower anodization time resulted in a more reliable mechanical structure and smaller pore dimensions. When the surface SNC and pores are smaller, as in the case of sample A1, the water droplets may build-up at the top layer more gradually as the humidity increases, leading to better linearity, at the expense of sensitivity. Here the water droplets remain within the top 10 % or so of d_{NPS} so that $d_{top} < 1\,\mu m$. Sample A3 has larger pore sizes (due to larger SNC) so that water diffuses deeper into the SNP layer ($\sim 1.2\,\mu m$), increasing d_{top}, thus decreasing the capacitance. The water also tends to build-up more suddenly on the top layer, causing non-linearity. Although sample A5 has smaller SNC dimensions than sample A3, the nanopore dimensions are much greater than those of the SNC. This would leave a larger percolated structure; here water diffuses across the whole of the NPS layer so that $d_{NPS} = d_{top}$. This decreases the capacitance, which remains lower than the other samples. Water droplets build-up much more rapidly on the surface as the humidity increases; however, the ease of water diffusion curtails a highly non-linear response.

The response times for reaching 63 % of the step humidity function are extended if the nanopore sizes are too small. This effect deteriorates sixfold for step decreases, since it is much harder for a drying gas to reach the inner nanopore structure. Samples A5 and A3 respond fastest to a step increase in humidity at 3.1 s·%rh^{-1}; their responses are only slightly delayed for step decreases. This makes their structures suitable for fast response humidity sensors.

Mechanical degradation gauged through a decrease in capacitance over 3 months ranged from ±4.0 nF from 20 %rh to 95 %rh. Samples A1 and A3 exhibited the least mechanical degradation. This shows that, after 60 min of anodization, the resulting SNP structure of the sensor is inherently unstable, making it unsuitable as a relative humidity sensor.

Hysteresis results showed the greatest hysteresis occurs at 95 %rh. A1 had the least hysteresis at 3.6 % and the maximum value is calculated to be 4.2 nF (4.6 %) for sample A5.

Thus, with the smallest average SNC size (and hence nanopore), sample A1 appears to contain the best structure, displaying adequate sensitivity, the most linear response, the least hysteresis, and a robust mechanical structure. The only disadvantage is that response time for step decreases in humidity is on average four times worse than the other structures; this may be improved by anodization procedures that slightly increase this pore diameter to ≤5 nm, since sample A2 has the next lowest pore diameter at 5.5 nm. The average dimension of the surface SNC size is 25 nm as determined by SEM; Raman analysis shows that this corresponds to an average sub-surface pore diameter of 4.5 nm.

References

1. M. Heinonen, M. Anagnostou, S. Bell, M. Stevens, R. Benyon, R. Anita Bergerud, J. Bojkovski, R. Bosma, J. Nielsen, N. Böse, P. Cromwell, A. Kartal Dogan, S. Aytekin, A. Uytun, V. Fernicola, K. Flakiewicz, B. Blanquart, D. Hudoklin, P. Jacobson, A. Kentved, I. Lóio, G. Mamontov, A. Masarykova, H. Mitter, R. Mnguni, J. Otych, A. Steiner, N. Szilágyi Zsófia, D. Zvizdic, Int. J. Thermophys. **33**, 1422 (2012)
2. D. Hudoklin, J. Bojkovski, J. Nielsen, J. Drnovšek, Measurement **41**, 950 (2008)
3. D. Hudoklin, J. Drnovšek, Int. J. Thermophys. **29**, 1652 (2008)
4. M. Heinonen, Measurement **17**, 183 (1996)
5. A. Uhlir, Bell Syst. Tech. J. **35**, 333 (1956)
6. L.T. Canham, Appl. Phys. Lett. **57**, 1046 (1990)
7. A.G. Cullis, L.T. Canham, Nature **353**, 335 (1991)
8. I. Schechter, M. Ben-Corin, A. Kux, Anal. Chem. **67**, 3727 (1995)
9. L. Seals, J.L. Gole, L.A. Tse, P.J. Hesketh, J. Appl. Phys. **91**, 2519 (2002)
10. S.E. Lewis, J.R. DeBoer, J.L. Gole, P.J. Hesketh, Sens. Actuators B **110**, 54 (2005)
11. Z.M. Rittersma, A. Splinter, A. Bödecker, W. Benecke, Sens. Actuators B **68**, 210 (2000)
12. M. Björkqvist, J. Salonen, J. Paski, E. Laine, Sens. Actuators A **112**, 244 (2004)
13. G. Di Francia, A. Castaldo, E. Massera, I. Nasti, L. Quercia, I. Rea, Sens. Actuators B **111**, 135 (2005)
14. R.L. Smith, S.D. Collins, J. Appl. Phys. **71**, R1 (1992)
15. H. Föll, M. Christophersen, J. Carstensen, G. Hasse, Mater. Sci. Eng. R **39**, 93 (2002)
16. X.G. Zhang, *Electrochemistry of Silicon and Its Oxide* (Kluwer/Plenum, New York, 2001)
17. O. Bisi, S. Ossicini, L. Pavesi, Surf. Sci. Rep. **38**, 1 (2000)
18. V. Lehmann, *Electrochemistry of Silicon: Instrumentation, Science, Materials, and Applications* (Wiley-VCH, Weinheim, 2002)
19. L. Canham (ed.) *Properties of Porous Silicon* (Institution of Engineering and Technology, London, 1997)
20. J.F. Morhange, G. Kanellis, M. Balkanski, Solid State Commun. **31**, 805 (1979)
21. J. Zi, H. Büscher, C. Falter, W. Ludwig, K. Zhang, X. Xie, Appl. Phys. Lett. **69**, 200 (1996)
22. F. Agullo-Rueda, J.D. Moreno, E. Montoya, R. Guerrero-Lemus, J.M. Martinez-Duart, J. Appl. Phys. **84**(4), 2349 (1998)
23. G. Faraci, S. Gibilisco, P. Russo, R. Penisi, Phys. Rev. B **73**, 033307–1 (2006)
24. S.K. Gupta, P.K. Jha, Solid State Commun. **149**, 1989 (2009)
25. B.K. Patel, R. Mythili, R. Vijayalaxmi, R.K. Soni, S.N. Behera, S.N. Sahu, Physica B **322**, 146 (2002)
26. Y. Kang, Y. Qiu, Z. Lei, M. Hu, Opt. Laser Eng. **43**, 847 (2005)
27. D. Chakravarty, B.V. Sarada, S.B. Chandrasekhar, K. Saravanan, T.N. Rao, Mater. Sci. Eng. A **528**, 7831 (2011)
28. H. Richter, Z.P. Wang, L. Ley, Solid State Commun. **39**, 625 (1981)
29. I.H. Campbel, P.M. Fauchet, Solid State Commun. **58**, 739 (1986)
30. Z. Sui, P.P. Leong, I.P. Herman, G.S. Higashi, H. Temkin, Appl. Phys. Lett. **60**, 2086 (1992)
31. G. Amato, V. Bullara, N. Brunetto, L. Boarino, Thin Solid Films **276**, 204 (1996)
32. L. Khriachtchev, M. Räsänen, S. Novikov, L. Pavesi, Appl. Phys. Lett. **85**, 1511 (2004)
33. N. Korsunska, B. Bulakh, B. Jumayev, L. Khomenkova, V. Yukhymchuk, T. Torchynska, Appl. Surf. Sci. **243**, 30 (2005)
34. K. Roodenko, I.A. Goldthorpe, P.C. McIntyre, Y.J. Chabal, Phys. Rev. B **82**, 115210 (2010)
35. J. Lu, X. Cheng, Y. Zhang, X. Zhu, Electrochim. Acta **55**, 5084 (2010)
36. M. Wesolowski, Phys. Rev. B **66**, 205207 (2002)
37. G. Korotcenkov, B.K. Cho, Crit. Rev. Solid State **35**, 153 (2010)
38. D.C. Giancolli, *Physics for Scientists and Engineers*, 4th edn. (Pearson, New York, 2009)
39. F.M. Liu, B. Ren, J.H. Wu, J.W. Yan, X.F. Xue, B.W. Mao, Z.Q. Tian, Chem. Phys. Lett. **382**, 502 (2003)
40. F. Zhong, Z. Jia, Physica B **411**, 77 (2013)
41. E. Burstein, *Raman Spectroscopy of Solids* (Defense Technical Information Center, Fort Belvoir, 1981)

42. V. Kumar, *Nanosilicon* (Elsevier, Oxford, 2008)
43. S. Oğuz Aytekin, R. Ince, A.O. Kodolbaş, Balkan Phys. Lett. **22**, 10 (2014)
44. MATLAB, Image Processing Toolbox User's Guide (2011–2014)
45. Y. Kim, J. Lee, Y. Kim, J. Kim, J. Semicond. Technol. Sci. **4**, 128 (2004)
46. Y. Wang, S. Park, J. Yeow, A. Langner, F. Müller, Sens. Actuators B **149**, 136 (2010)
47. H. Kim, N. Cho, Nanoscale Res. Lett. **7**, 408 (2012)
48. D. Hudoklin, J. Šetina, J. Drnovšek, Int. J. Thermophys. **33**, 1595 (2012)
49. C.R.B. Miranda, M.R. Baldan, A.F. Beloto, N.G. Ferreira, J. Braz. Chem. Soc. **19**, 769 (2008)
50. P. Granitzer, K. Rumpf, Materials **3**, 943 (2010)
51. Z.C. Feng, R. Tsu (eds.), *Porous Silicon* (World Scientific, Singapore, 1994)